Spatiotemporal Mapping of Concentration Polarization Induced pH Changes at Nanoconstrictions

Junyu Mai, Hanna Miller, and Anson V. Hatch*

Department of Biotechnology and Bioengineering, Sandia National Laboratories, Livermore, California 94551, United States

ABSTRACT Under an applied electric field, concentration polarization (CP) arises from ion permselectivity of most nanoporous materials and biological ion channels. We present novel methods to quantitatively assess CP-induced spatiotemporal changes of pH that may significantly impact transport dynamics, device functionality, and physicochemical properties of molecular analytes in devices with nanofluidic constrictions. We measured pH fluctuations of >1.5 pH units and changes extending over 100's of micrometers from nanoconstrictions. The degree of change depends on key system parameters including buffer composition, surface charge, and strength of electric field. The results highlight the importance of neglected contributions of pH changes, and the approach can aid characterization and manipulation of mass transport in nanofluidic systems.

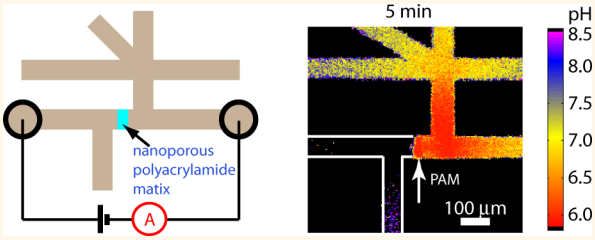

KEYWORDS: nanoporous structure · pH mapping · concentration polarization · nanofluidic transport · preconcentration membrane · electrokinetic transport

Applying electric fields is an effective means of manipulating fluid and molecular transport through nanofluidic channels or nanoporous media for diverse applications including ion exchange, molecular enrichment, fractionation, filtration, and sensing. For example, various nanoporous structures have been created using etched nanochannels or photopatterned nanoconstrictions to enrich proteins or nucleic acids in a fluidic sample[1−4] and to improve the detection limits[5−7] of molecular sensing devices. For many such applications, it is important to understand the impact of electric-field-induced concentration polarization (CP) on transport behavior and physical and chemical properties of the system.[8−11] CP commonly arises as electrical current flows through nanofluidic device elements interfaced with micro or larger-scale compartments. Within nanoconstrictions, the concentration of ions in the electric double layer (EDL) shielding surface charge becomes significantly higher than in the bulk fluid. As a result, EDL carries a significant portion of electrical current through the nanofluidic element, and counterions (to EDL) accumulate at the micro/nano interface, where EDL ions selectively enter the nanochannel. The counterions are also depleted on the other side of nanoconstrictions, where EDL ions exit. Conditions favoring the occurrence of CP may be best described by the Dukhin number,[12] a nondimensional constant comparing electrical conductance of the bulk, G_b, to surface conductance, G_s. When G_s is similar to or greater than G_b, permselectivity and CP generated by the nanofluidic element can lead to significant temporospatial fluctuations in electrical current, ion distribution, transportation, and other system performance parameters. In natural biological systems, the transport of ions driven by the electropotential established across the plasma membrane through pore-forming ion channels is also regulated by the permselectivity imparted by charged amino acid residues lining the channel surface.[13,14] Studies elucidating the complexities of the regulation of ion flux across cell membranes are critical to understanding the structure−function relationship of the ion channels and its implication to disease development and human health.[15,16]

Extensive theoretical and experimental studies have focused on CP across synthetic

* Address correspondence to ahatch@sandia.gov.

Received for review August 30, 2012 and accepted October 12, 2012.

Published online October 13, 2012
10.1021/nn304005p

nanoporous membranes, packed beds, and micro/nanofluidic devices.[10,17−23] It has been found that a variety of factors, including surface charge, buffer ion strength, and electric field strength, can affect the extent of CP and eventually device performance. For instance, adverse effects of CP on a nanoporous preconcentration membrane include temporal losses in electrical currents, decreases in electrophoretic loading efficiencies, zones of high electrical resistance, and poor reproducibility.[24] In microfluidic isoelectric fractionation devices, CP can cause undesired entry of proteins targeted for exclusion into the pH-specific nanoporous membranes.[25] A detailed understanding is still severely limited by theoretical complexities and experimental challenges. Particularly, CP-induced change of pH at nanoporous structures is generally neglected,[8,12] and experimental investigation on this important topic has been limited. Dynamic, localized changes in acid−base chemistry caused by permselectivity and ion accumulation and depletion at the nanoconstrictions may contribute significant nonlinear behaviors, affecting important system properties coupled to pH. Adding to the complexity, the surface charge of nanomaterials may also be titrated in the process, dynamically altering the character of EDL and CP.[26] The combined effects may dramatically alter the physical properties and transport of biological analytes and other soluble species that have titratable charged groups. For example, local pH determines the charge state of a protein analyte and affects its electromobility. In addition, change of local pH may affect kinetics of chemical reactions and molecular binding affinities and directly interfere with molecular recognition and sensing reactions designed to occur in the vicinity of a nanoconstriction.

RESULTS AND DISCUSSION

In this study, we developed a novel method to quantitatively map CP-induced pH changes inside a functional micro/nanofluidic system. Using a dual-emission pH-sensitive fluorescent dye, carboxyseminaphthorhodafluor (SNARF), we obtained high-resolution spatiotemporal mapping of pH across nanoconstrictions and surrounding microchannels. We quantitatively investigated the dynamic change of local pH as electric fields were applied to induce CP across a nanoporous structure and compared the change of pH to the degree of CP as indicated by the drop of current through the same structure. We measured pH fluctuations of >1.5 pH units and changes extending over 100's of micrometers from nanoconstrictions. Possible mechanisms causing the shift of pH are discussed on the basis of results generated in different experimental conditions. Specifically, we found that (1) electric field strengths, (2) ion strength and composition of the running buffer, and (3) surface charges of the nanoporous structure are significant factors affecting both the pH and the CP at the nanoconstrictions. We also suggested preliminary models to understand the complicated interplay of multiple factors leading to the related phenomena at the micro/nano interface.

Experimental System and Calibration. Our device configuration shown in Figure 1A has a narrow 50 μm wide nanoporous polyacrylamide matrix (PAM) fabricated within isotropically etched glass microchannels (30 μm deep × 100 μm wide) by *in situ* photopolymerization. The average size of nanopores is controlled as a function of monomer concentration in the precursor solution, and the surface charge can be modulated by copolymerization of cationic and/or anionic monomers. The average diameter of PAM nanopores studied is ~1 nm for the relatively high concentration of acrylamide monomer and bisacrylamide cross-linker (44% T, 10% C). The pores are small enough to exclude biomolecules larger than the pore diameter including proteins and nucleic acids,[27] which will stack at the PAM with applied electrophoretic driving forces.[24] The small pore size and pore surface charge can result in significant EDL conductance through the matrix. On both sides of the PAM, the effective microchannel diameter is orders of magnitude larger than the pores, thus establishing CP conditions with high EDL conductance in the nanoporous structure and negligible EDL conductance in the microchannel.

As the acrylamide and bisacrylamide monomers are neutral, we introduced 0.3% (molar ratio) of either negatively or positively charged acrylamido Immobiline monomers in the total monomer solution to modulate permselectivity of the resulting polyacrylamide nanoconstrictions, denoted here as PAM^- and PAM^+, respectively. We note that PAM without addition of charged monomer exhibits a slight negative charge linked to polymer hydrolysis, resulting in trends similar to PAM^-. Nanofluidic materials frequently exhibit negative surface charge, where permselectivity of nanoconstrictions exhibits CP with anion enrichment on its cathode side and anion depletion on the anode side.[8,12,19,20]

An electric field was applied across the PAM nanoconstriction (Figure 1A) directed on each side through only one of the intersecting microchannels. The channels leading to fluid reservoirs where no electric field was applied provide insight to the contributions of diffusive flux of ions that becomes more dominant relative to electrophoretic transport in these side channels. Cross-matrix current was monitored once the electric field was applied. Note that the reported field values are averages between two electrodes across the long channel (20 mm) and relatively short matrix (0.05 mm) segment. With CP, the field distribution is not uniform across the channel and dynamically changes over time. The local resistance across CP-induced depletion zones can become substantially higher than other segments of the channel, resulting

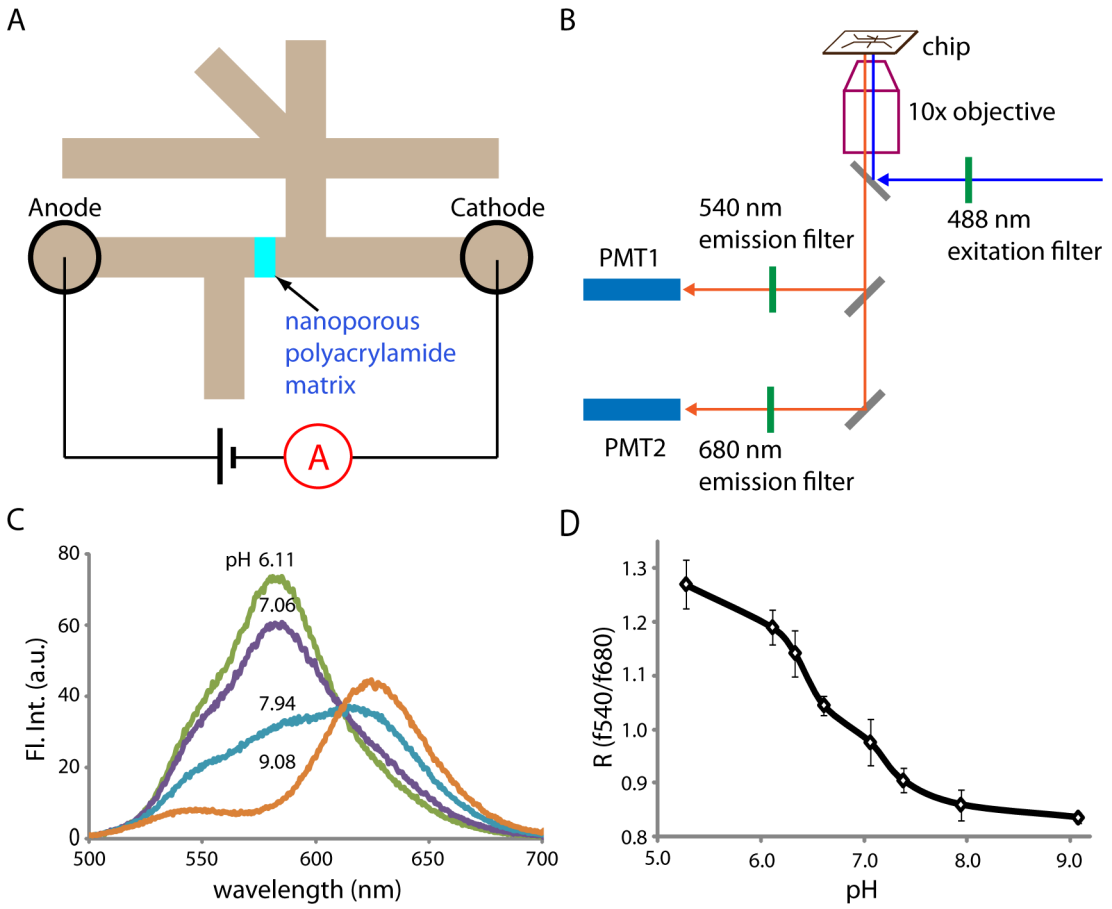

Figure 1. Experimental systems. (A) Layout of the glass chip used for pH mapping across a 50 μm long nanoporous polyacrylamide matrix (PAM) fabricated inside a 30 μm deep and 150 μm wide microchannel (not to scale). SNARF is mixed in channels filled with running buffer and 1% methyl cellulose. As a constant voltage is applied through two electrodes, current across the nanoporous matrix is monitored concurrently as the fluorescent signals of SNARF are measured. (B) The chip is mounted on an inverted confocal microscope sample stage. The 1 mm × 1 mm area surrounding the PAM is excited at 488 nm in a scanning mode. Dual emission images are collected simultaneously by two photomultiplier tubes (PMTs) every 30 s. (C) Emission spectra of SNARF (20 μM) excited at 488 nm in PBS titrated to different pH. (D) On-chip calibration of SNARF emission ratio $R = f_{540}/f_{680}$ *vs* pH.

in substantially higher localized field strength and limiting current.

Phosphate-buffered saline (1× PBS, 10 mM Na phosphate, and 150 mM NaCl, pH 7.5), a standard buffer widely used for bioanalysis, served as a representative solution for evaluation. Phosphate buffer without added salt (1× PB, 10 mM Na phosphate, pH 7.5) was also evaluated to examine the influence of ionic strength.

To examine dynamic on-chip pH changes induced by CP across PAM, we mixed 20 μM SNARF into the running buffer loaded into the device and simultaneously recorded fluorescent images at SNARF's two emission peak wavelengths (Figure 1B). SNARF is well characterized and developed for intracellular pH measurement.[28,29] It was also used for single-point pH monitoring in capillary electrophoresis.[30] In the buffers we used, both protonated and unprotonated SNARF, with emission peaks at 540 and 680 nm, respectively, when excited at 488 nm (Figure 1C), are negatively charged (Supporting Information Scheme S1) and will migrate toward the anode when an electric field is applied. Since the ratio of the two emission intensities, not the relative value of any single fluorescent intensity, is used to calibrate and calculate local pH (Figure 1D), quantitative measurement can be obtained despite spatially fluctuating dye concentration caused by molecular accumulation and depletion during CP events inside the micro/nanofluidic devices. Although adding complexity to the imaging process compared to nonratiometric pH-sensitive dyes such as fluorescein,[31] ratiometric measurement is suited for measuring pH when dynamic and unpredictable changes in the dye concentration occur.

Time-Lapse 2D pH Mapping Across Polyacrylamide Matrix. We find that temporospatial pH changes at PAM$^-$ nanoconstrictions can be significant with PBS buffer and an electric field as low as 25 V/cm, as shown in Figure 2A. After application of the electric field at 25 V/cm for 30 s, pH at the cathode side of the PAM$^-$ decreased from the starting value of 7.6 to ~6.0. The affected region of enrichment (with pH lower than 7.4)

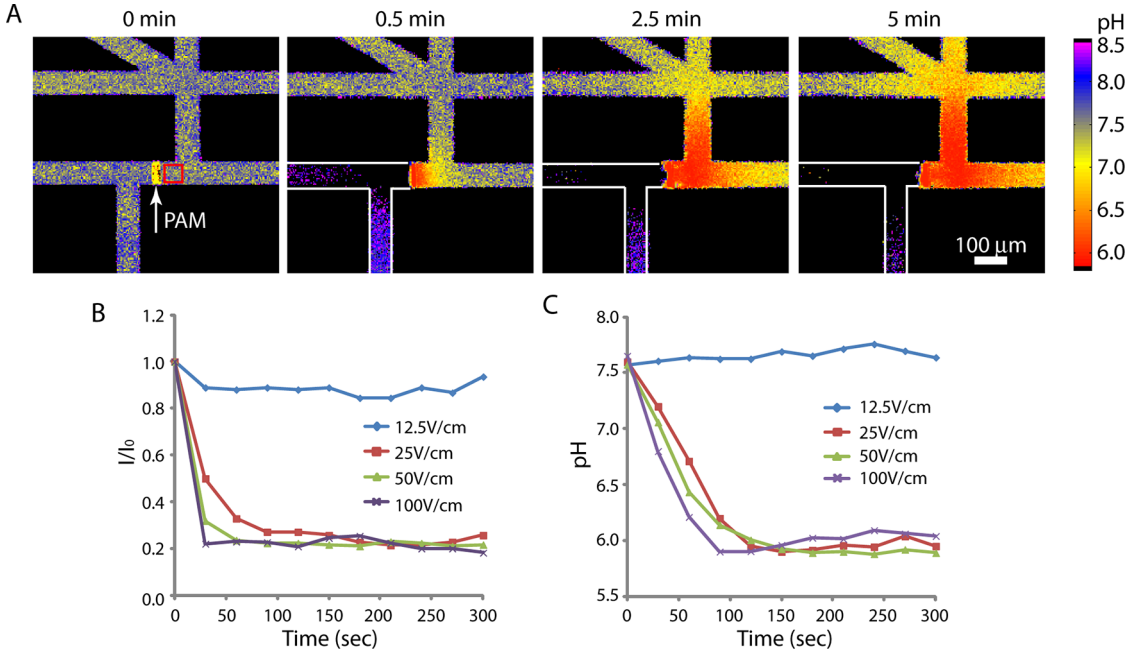

Figure 2. Time-lapse 2D pH mapping of PAM$^-$. (A) An electric field of 25 V/cm is applied across a nanoporous PAM$^-$ nanoconstriction fabricated with neutral acrylamide monomers. Substantial pH drop occurs on the cathode side of the matrix within 30 s, and the affected area propagates to >700 μm away from the PAM$^-$ within 5 min. On the anode side of the PAM$^-$, depletion of SNARF molecules along with buffer ions prevents mapping of pH in this zone. Further away from the PAM$^-$, where the fluorescent signal is detectable, pH increases to >8.5 within 30 s. (B) Faster decrease of electrical current through nanoconstrictions (normalized by starting current I_0) with increasing electric field strength. (C) Faster drop of pH on the cathode side of PAM$^-$ with increasing electric field strength. Each pH value is the average of the 80 μm $\times$ 80 μm area by the PAM$^-$, as shown by the red square in (A).

expanded from 50 μm beyond the PAM$^-$ at 30 s to 700 μm at 5 min into the branching channels. An ion depletion zone was generated on the anode side of the PAM$^-$, where SNARF dye was quickly depleted as it was driven by the electric field toward the anode along with other anions while not being replenished due to permselectivity of the nanoporous matrix (Supporting Information Figure S1). SNARF fluorescence was too weak for pH measurement in the heart of the ion depletion zone, but significant increase in pH above 8.5 was observed closer to the edges of the depletion zone. The affected area was much larger on the depletion side with a pH higher than 8.5 at more than 500 μm away from the PAM$^-$ within 30 s at 25 V/cm. We cannot measure whether pH changes were even more extreme in the SNARF-depleted regions, but pH gradients at the edges suggest higher pH extremes in this region. Concurrent recording of electrical currents showed that the current dropped ~70% within 2 min after application of the electric field (Figure 2B), which is a standard indication of CP.

The strength of CP (inferred from rates and magnitude of current drop) and rates and extent of pH changes all tended to increase with increasing electric field. Field strength dependencies were measured over the range of 12.5 to 100 V/cm, as shown in Figure 2B and C. One exception where CP was not indicated was with PAM$^-$ at 12.5 V/cm; no measurable changes in current were observed over 10 min, and pH also remained relatively stable. With PBS at 25 V/cm, the current dropped more than 50% within 30 s. As field strength was increased, the electrical current decayed at a faster rate to a limiting current. Following a similar trend, pH decreased on the cathode side of the PAM$^-$ as field strength was increased, but it took more time for pH to reach a stable state extending into the microchannels than for electrical current stablilization.

Effect of Buffer Composition on Concentration Polarization and Change of pH. We find a strong dependency of CP-induced pH changes on buffer properties. Phosphate buffer for the pH range evaluated consists of monovalent hydrogen phosphate anion and its conjugate base dihydrogen phosphate anion adjusted to set and regulate the pH. Phosphate has some capacity to regulate pH in response to local changes in ionic balance by protonation/deprotonation according to eq 1:

$$H_2PO_4^- \leftrightarrow HPO_4^{2-} + H^+; \quad pK_a = 7.2 \qquad (1)$$

The acid dissociation constant (pK_a 7.21) relevant in the pH range studied here describes the dissociation of dihydrogen phosphate ($H_2PO_4^-$) to hydrogen phosphate (HPO_4^{2-}) and H^+. The ionic strength of the buffer solution also influences pH in accordance with Debye–Huckel theory of interionic forces including significant contributions from NaCl (150 mM at 1×) in PBS, serving in biological applications to achieve isotonicity with cells and avoid osmotic shock.

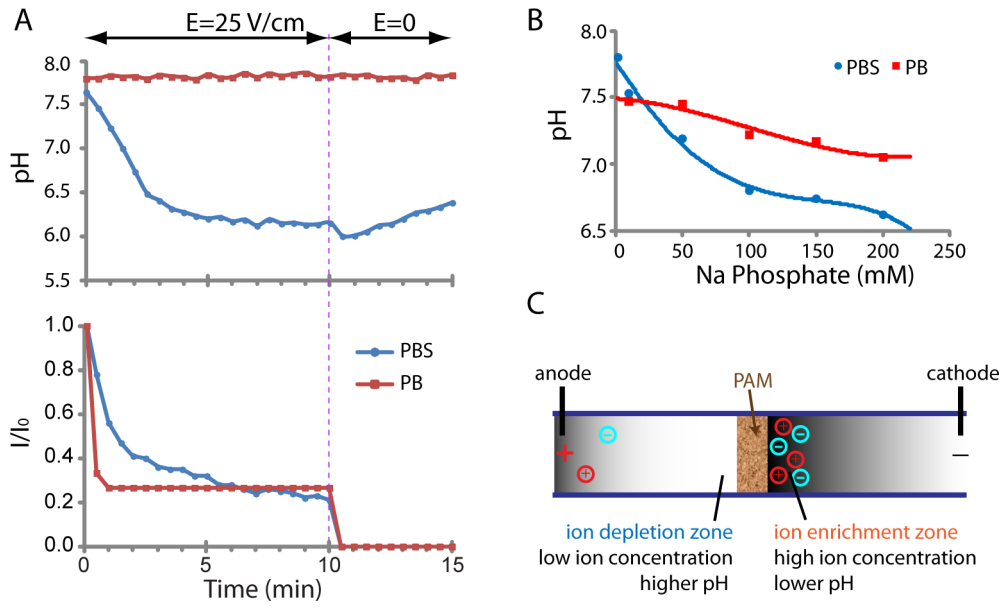

Figure 3. Effect of buffer composition on concentration polarization and change of pH: comparison between PBS and PB. (A) Change of pH on cathode side of PAM$^-$ and cross matrix current with PBS or PB. The pH and current are measured concurrently with electric field at 25 V/cm applied. Each pH value is the average of the 80 μm × 80 μm area on the cathode side of the PAM$^-$, as shown by the red square in Figure 2A. Purple dotted line indicates the time when the electric field is turned off. As soon as the applied field was removed, the pH slowly re-equilibrated back toward the starting pH due to diffusive transport. (B) Change of bulk solution pH at different dilutions of 20× PBS (200 mM Na phosphate and 3 M NaCl) and 20× PB (200 mM Na phosphate), indicating a more significant decrease of pH with higher concentration of PBS than with PB. (C) Schematic of the suggested model explaining the decrease of pH caused by increasing concentration of ions in the ion enrichment zone induced by CP in PBS. With PB, ion concentration in the ion enrichment zone is much lower than in PBS; therefore pH remains relatively stable despite a stronger CP, as indicated by a faster drop of current.

To investigate the effect of ionic strength and buffer composition on CP-induced changes in local pH, we compared pH maps across PAM$^-$ with two different buffer systems at 25 V/cm: PBS (10 mM Na phosphate and 150 mM NaCl) and phosphate buffer (PB) (10 mM Na phosphate without added salt). Fluorescent imaging of SNARF confirms a depletion zone on the anode side of PAM$^-$ in both cases. Change of electric current shown in Figure 3A indicates a stronger CP with lower ionic strength PB than with PBS, which is expected based on the Dukhin number theory. Lower ion concentration of PB increases the relative number of ions in the EDL compared to the bulk fluid, and as a result, a more dominant EDL conductivity leads to a stronger CP and faster current drop. However, a stronger CP does not necessarily correlate with a stronger pH change, as our data also show that pH in the enrichment zone (cathodic side of PAM$^-$) with PB was stable, whereas a large drop in pH (from 7.6 to 6.0) was observed with PBS (Figure 3A).

To understand these different patterns of pH change, we analyze two aspects of changing distribution of solution ions that influence pH: (i) local changes in the total ionic strength and (ii) local changes in the relative distribution of different ionic species associated with differential flux of cations *vs* anions across the nanoporous matrix.

It is known that changing the ionic strength of PBS can result in significant changes in solution pH due to ion interactions.[32] To assess the relative influence of ionic strength changes, bulk solution pH was measured at different dilutions of the 20× PBS stock (200 mM Na phosphate and 3 M NaCl). Figure 3B shows that the pH increases from 6.5 at full 20× stock concentration to 7.5 at the 1× PBS level loaded into chips and reaches a maximum of ~7.8 when diluted to 0.2× (2 mM of Na phosphate and 30 mM NaCl). Further dilution of PBS decreases the pH toward the unbuffered pH of water. Increasing the ionic strength to a similar level by adding NaCl to 1× PB results in a similar change of pH (pH = 6.5 with 1.4 M NaCl). Compared to PBS, a solution of 10 mM PB has substantially lower initial ionic strength. Equivalent increases in the concentration of PB alone yields a much smaller decrease of pH, and it would require order of magnitude higher concentration factors to approach similar ionic strength contributions influencing pH (Figure 3B). These bulk solution measurements give some indication of the pH extremes that might be reached in a simple ion dilution and enrichment model of CP, as depicted in Figure 3C. For example, greater than 20-fold enrichment of ionic strength from the initial 1× PBS is required to approach the pH minimum measured within the enrichment zone on the cathode side of the PAM$^-$. We notice that a simple model of ion dilution in the depletion cannot explain the pH maximum measured on the anode side of the PAM$^-$ as, at most, a maximum pH of 7.8 is expected at ~5-fold dilution of 1× PBS. However pH

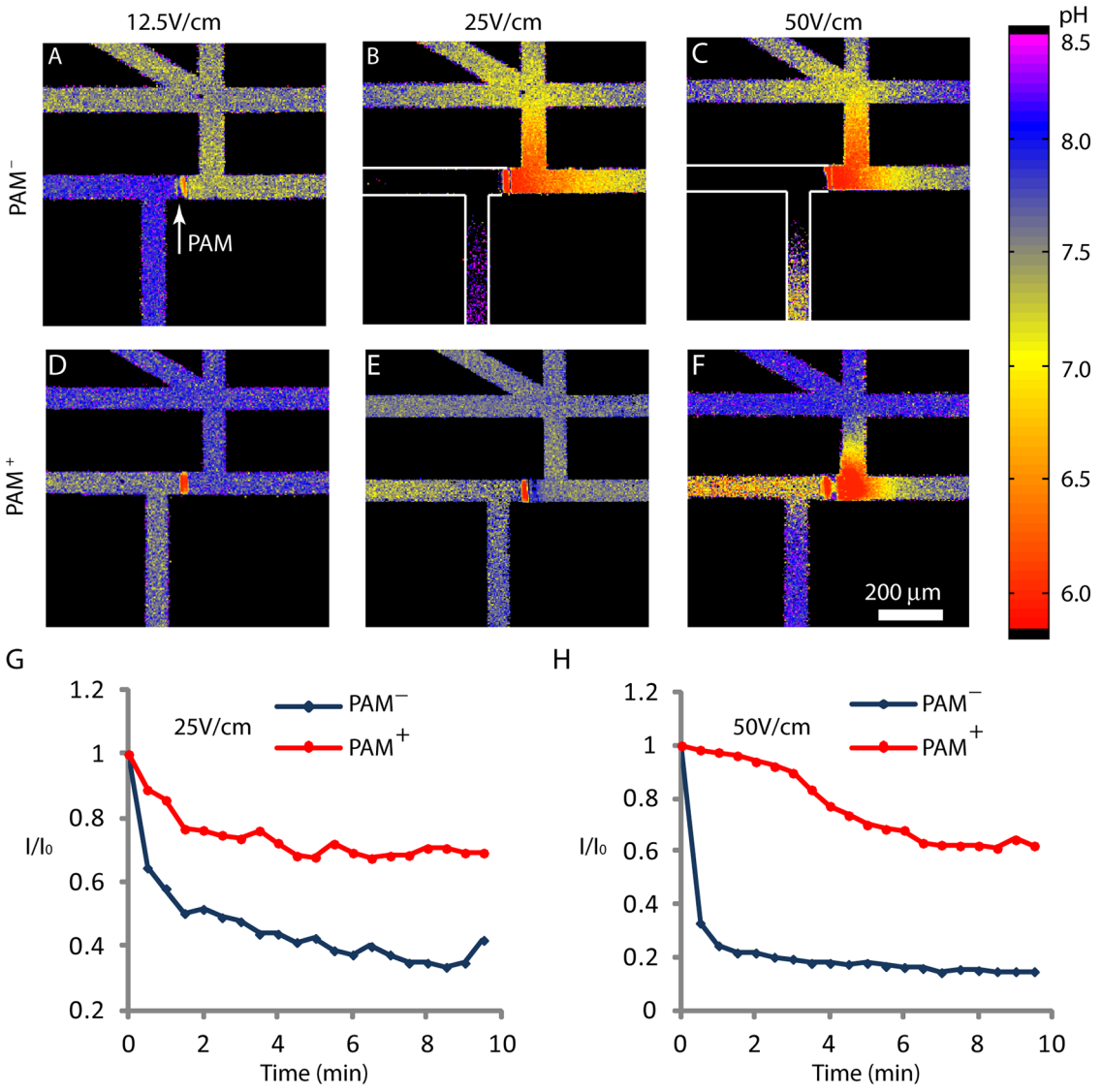

Figure 4. Change of pH and current across positively and negatively charged nanorestrictions (PAM^+ and PAM^-) at different electric field strength. PAM^+ and PAM^- are fabricated with the addition of 0.3% charged Immobiline monomers. (A–F) pH images measured 10 min after application of electric field at indicated strength in PBS buffer. (G, H) Normalized cross-matrix current measured at 30 s increments after electric field was applied across PAM^+ and PAM^-.

values above 8.5 were measured. We also note that the effect of ionic strength on pH is different depending upon the buffer composition. Our measurements of the pH of several commonly used buffers for electrophoresis are summarized in Supporting Information Table S1, demonstrating different buffers have different levels of pH change in response to the increase of salt and total ion concentration. Although CP-induced pH changes are complicated beyond simple ionic strength consideration, the ionic strength of initial running buffer is clearly an important factor to consider in attempting to minimize or enhance CP-induced pH changes.

Differential ion flux is important to consider, especially in light of measured pH extremes. The magnitude of CP-induced pH shifts can be explained by shifts in acid/base equilibria linked to permselectivity of the matrix for the ionic species involved (Figure 5A). Between pH 5 and 9, the dominant forms of phosphate buffering ions are $H_2PO_4^-$ and HPO_4^{2-} in eq 1. This coupled with the acid/base equilibrium of water,

$$H_2O \leftrightarrow H^+ + OH^-; \quad pK_a = 7 \qquad (2)$$

and charge and mass conservation dictates pH shifts in response to differential transport of ions across the matrix. On the cathode side of the PAM^-, anions Cl^-, $H_2PO_4^-$, and HPO_4^{2-} accumulate in the anion enrichment zone in front of the negatively charged matrix due to cation permselectivity of the nanopores. Meanwhile cations including Na^+ continue to migrate through the matrix and toward the cathode. With PBS, OH^- is generated and H^+ decreased in the anion depletion region to balance higher local Na^+. The $H_2PO_4^-$ and HPO_4^{2-} ions are depleted in this region leaving it more

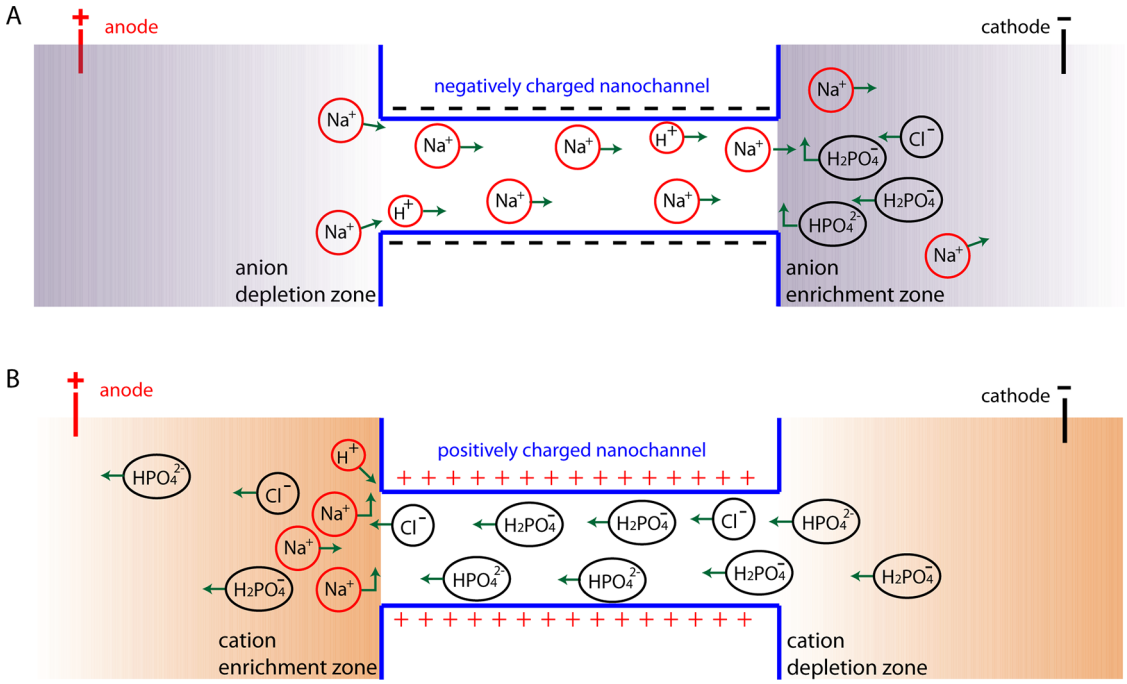

Figure 5. Schematic of the suggested model explaining the change of pH across negatively and positively charged nanoconstrictions. (A) On the cathode side of negatively charged nanoconstrictions, a high concentration of phosphate ions in the anion enrichment zone leads to increased concentration of H^+ and a lower pH. On the anode side, depletion of phosphates in the anion depletion zone leads to higher pH. (B) With positively charged nanoconstrictions, because buffering phosphate ions can cross nanoconstrictions through the EDL, the pH is more stable even with electric-field-induced CP.

susceptible to pH fluctuation. On the cathode side, continuing flux of Na^+ but accumulation of Cl^- and phosphate anions pushes local pH downward as H^+ increases balancing charge. However, the titration of HPO_4^{2-} to $H_2PO_4^-$ buffers against pH changes to some extent. With PB as compared to PBS, the substantially lower Na^+ and lack of Cl^- lessen tendencies for pH change on both sides of the matrix, and a higher relative concentration of buffering ions tends to stabilize the pH in the enrichment zone.

Time-Lapse pH Mapping across Positively and Negatively Charged Polyacrylamide Matrix. To study the impact of switching the polarity of surface charge on CP-induced pH changes, we compared positive and negative surface charge variations in Figure 4. Snapshots of pH maps of PAM^- and PAM^+ in PBS were measured at 10 min after application of the electric field (Figure 4A–F). The change of pH across PAM^+ was similar to PAM^- in that the pH tended to drop on the cathode side of the matrix, but there were notable differences (Figure 4D–F). At a low electric field of 12.5 V/cm, PAM^+ maintained a stable pH map (Figure 4D). At a higher voltage of 25 V/cm the change of pH is relatively mild, with only a narrow zone (~50 μm) of higher pH on the cathode side of the matrix in the cation depletion region (Figure 4E). At a stronger electric field of 50 V/cm, the pH on the cathode side of PAM^+ decreased sharply to ~6.0 in the depletion region, whereas on the anode side, the pH also decreased but at a smaller level to ~6.6. The magnitude of pH shifts and the size of regions affected are much smaller than observed for PAM^- (Figure 4F). Current drop at 25 and 50 V/cm across PAM^+ were less than half the drop across PAM^- (Figure 4G, H), indicating weaker CP.

The observed changes with PAM^+ are not aligned as well with a simple model of ionic strength dependence since the pH shifted opposite the trend expected in the ion depletion region (now on the cathode side). Here again coupled effects of ionic strength and differential transport of anions *vs* cations as illustrated in Figure 5B must be considered to explain the local pH shifts. At PAM^+ the permselectivity is reversed compared to PAM^-, and thus negatively charged phosphate buffering anions $H_2PO_4^-$ and HPO_4^{2-} along with Cl^- are carried through the EDL. The depletion and enrichment regions are also reversed across the matrix with cations (Na^+) instead of anions being excluded and therefore enriched on the anode side and depleted on the cathode side. The charge neutrality in the microchannels is maintained by the acid/base chemistry (eqs 1 and 2). Overall, with a more stable concentration of phosphate buffering ions across the PAM^+ and in the depletion region, the pH is better regulated. In the enrichment region (on the anode side of PAM^+), the accumulation of Na^+ is expected to shift the acid/base equilibrium to higher pH, while higher ionic strength is expected to lower the pH. The pH is lowered by a modest amount at 50 V/cm, indicating that the ionic

strength effect dominates somewhat at the higher field strength. In the depletion zone, dilution of ions can increase PBS pH (up to ~5-fold dilution levels). However, as Na^+ is depleted, the acid/base equilibrium is expected to shift pH lower, while the phosphate buffer (not depleted in this case) would attenuate the shift in pH to some extent. The most significant change in the depletion region at 50 V/cm is a drop in pH to ~6, implicating differential transport of ions as the dominant factor.

The experimental model studied here focused on anionic buffer ions resulting in smaller pH changes and lower current drop when nanopore surface charge is positive. If the buffering species counters surface charge and is conducted through the EDL, buffering capacity can serve to reduce the extent of current drops and pH changes on both sides of the nanoconstriction. Some buffer compositions such as Tris-glycine buffer are buffered by both cationic and anionic species, further emphasizing the complex dependence of dynamic CP and locally induced pH changes on buffer choice and ionic composition. An improved understanding will help guide the choice of running buffer and surface charge characteristics to better predict and mitigate or enhance CP-induced effects to suit an application.

CONCLUSION

Although characterization of the results is based on a highly simplified model and many aspects of the observed phenomenon are coupled, this is the first quantitative study of often neglected changes of pH at nanoconstrictions. As CP-induced pH shifts have been difficult to account for both theoretically and experimentally, this approach helps in identifying the extent of pH shifts that may occur and in mapping contributions of several factors. The magnitude of pH changes at the micro/nano interface caused by CP as demonstrated here can significantly impact the behavior and performance of nanofluidic devices. With ratiometric temporospatial pH mapping, dynamic and unpredictable pH changes can be qualitatively and quantitatively analyzed across a wide range of micro/nanosystem parameters. The models depicted here in Figure 3C and Figure 5 include multiple coupled mechanisms contributing to pH changes at nanoconstrictions. A descriptive correlation of multiple factors with CP including dependence on field strength, buffer composition, and surface charges will help facilitate more in-depth theoretical and experimental study in the future.

METHODS

Reagents. Carboxy SNARF-1 and *N*,*N*′-methylenebisacrylamide were from Invitrogen (Calsbad, CA, USA). Acrylamide solution (40%), 3-(trimethoxysilyl)propyl methacrylate (98%), methylcellulose, sodium phosphate, and glacial acetic acid were from Sigma (St. Louis, MO, USA). 2,2′-Azobis[2-methyl-*N*-(2-hydroxyethyl)proprionamide] photoinitiator (VA-086) was from Wako Chemicals (Richmond, VA, USA). PBS buffer (20×), Tris-buffered saline (20×), and borate buffer (20×) were from Thermo Scientific (Rockford, IL, USA). Immobiline solutions (0.2 M) were from Fluka (Buchs, Switzerland). Bogen's Universal pH indicator was from The Science Company (Denver, CO, USA).

Device Fabrication. A glass (fused silica) microfluidic device with nanoporous polyacrylamide matrix photopolymerized *in situ* was fabricated as previously described.[24,33] Briefly, the devices were designed in-house and were fabricated at Caliper Life Sciences (Hopkinton, MA, USA) using standard wet etching techniques with chromium masks fabricated by Photo Sciences Inc. (Torrance, CA, USA). Microchannels were 30 μm deep throughout the chip, with 500 μm diameter circular holes drilled into the top layer of the device to allow access to the channels. We first coated the channels with methacrylate-terminated silane *via* a 30 min incubation with a 2:3:5 (v/v/v) mixture of 3-(trimethoxysilyl)propyl methacrylate, glacial acetic acid, and deionized water. The channels were then rinsed twice with methanol and twice with DI water, thoroughly dried with a vacuum, and stored dry until PAM fabrication. For nanoporous PAM fabrication, the devices were loaded with a mixture of acrylamide/bisacrylamide cross-linker (44% T, 10% C, where % T represents the total monomer mass concentration, and % C represents the mass percentage of bisacrylamide cross-linker to total monomer) and 2 mg/mL VA-086 photoinitiator. For negatively charged and positively charged PAMs, 20 mM pK_a 3.1 and pK_a >12 Immobiline was added into the monomer mixture, respectively. After about 10 min for the liquid inside the channel to reach a quiescent state, 30 μm wide PAMs were polymerized in the device by exposure to a shaped UV laser beam (355 nm frequency-tripled Nd:YAG). Excess monomer solution was removed *via* vacuum; channels were rinsed twice with methanol. Finally, we coated the channels of the chips with linear polyacrylamide by loading the channel with a solution of 4% acrylamide and 2 mg/mL VA-086 photoinitiator and exposing the device to a 100 W flood UV lamp for 6 min. Following exposure, excess solution was removed *via* vacuum, and the channels were flushed twice with methanol and filled with water until use.

Device Operation. Channels was filled with appropriate running buffer (PBS or PB) mixed with 1% methylcellulose (MC) and 200 μM SNARF *via* capillary wicking. MC was added to minimized electroosmotic flow.[33] The chip was then mounted onto a custom-made manifold for easy access to the channels.[34] About 80 μL of channel solution was added in each channel reservoir. Platinum electrodes were inserted into each reservoir and connected to a custom-made programmable high-voltage power supply. A 25 V/cm (or as indicated) electric field potential was applied between the cathode and anode port for a preprogrammed duration of time. The cross PAM current was measured from the same power supply every 30 s. The field was directed on each side of the PAM through only one of the intersecting microchannels (Figure 1A). The intersecting microchannels help in photopolymerizing the PAM, allowing quick rinsing of unpolymerized monomer solution, and are also important for integrated analytical uses facilitating delivery of different sample analytes, chemical reagents, and buffers to the PAM and subsequent redirection of processed samples for downstream analysis.

SNARF Emission Spectra Measurement. SNARF emission spectra were measured with 488 nm excitation using a fluorescent spectrometer (Perkin-Elmer, LS55) in PBS and phosphate buffer titrated from pH 6 to 9.

Onchip SNARF Calibration. For time-resolved pH mapping in a micro/nanofluidic device, calibration was performed by filling

representative microchannels with buffer solutions titrated over a range of pH and measuring fluorescent responses with the imaging system (when CP is not induced). Images of fluorescent emission at 540 and 680 nm of the channel with 488 nm excitation were acquired using a confocal microscope (BioRad LaserSharp2000) and a krypton/argon laser. The optical system setup is illustrated in Figure 1B. Emission filters at 540 ± 32 and 680 ± 32 nm were chosen to optimize the ratiometric imaging response measured as

$$R = \frac{f_{540}}{f_{680}}$$

where f_{540} and f_{680} are the background-subtracted fluorescence emission intensity simultaneously measured using two PMTs. The calibration curve of *R vs* pH shown in Figure 1D is based on fitting a second-order polynomial equation by least-squared linear regression

$$\mathrm{pH} = 4.3R^2 - 9.2R + 10.8$$

which was used to correlate a measured *R* value to a specific pH value between pH 5.8 and 8.5 pH mapping.

Dynamic pH Mapping. The manifold with the chip filled with SANRF in the channel and electrodes connected to the power supply was mounted on a confocal microscope (Bio-Rad) sample stage. After the electric field was applied, dual emission images at 540 and 680 nm of the area of interest (1 mm × 1 mm) were scanned simultaneously every 10 s. Scanning time for each set of dual images was within 1 s. Afterward, we analyzed the images and generated pH maps using computer software ImageJ (http://rsbweb.nih.gov/ij/) and Matlab (Mathworks) based on the ratio of fluorescent intensity of each pixel measured at 540 and 680 nm and the pH *vs R* calibration curve.

Bulk Solution pH Measurement. We measured the pH of bulk buffer solution with a benchtop electronic pH meter (Mettler Toledo, Seven Multi InLab Micro) and further verified the result with several colorimetric pH indicators: neutral red (pH 6.8−8.0), bromothymol blue (pH 6.0−7.6), and Bogen's Universal pH indicator (pH 1−12).

Conflict of Interest: The authors declare no competing financial interest.

Acknowledgment. We thank Dr. R. Meagher for insightful discussion. This project received support from the Defense Threat Reduction Agency-Joint Science and Technology Office for Chemical and Biological Defense (IAA number DTRA10027IA-3167) and from Sandia's Laboratory Directed Research and Development Program. Sandia is a multiprogram laboratory operated by Sandia Corp., a Lockheed Martin Co., for the United States Department of Energy under Contract DE-AC0494AL85000.

Supporting Information Available: Supporting Figure S1, Scheme S1, and Table S1. This material is available free of charge *via* the Internet at http://pubs.acs.org.

REFERENCES AND NOTES

1. Khandurina, J.; Jacobson, S. C.; Waters, L. C.; Foote, R. S.; Ramsey, J. M. Microfabricated Porous Membrane Structure for Sample Concentration and Electrophoretic Analysis. *Anal. Chem.* **1999**, *71*, 1815–1819.
2. Wang, Y. C.; Stevens, A. L.; Han, J. Y. Million-Fold Preconcentration of Proteins and Peptides by Nanofluidic Filter. *Anal. Chem.* **2005**, *77*, 4293–4299.
3. Foote, R. S.; Khandurina, J.; Jacobson, S. C.; Ramsey, J. M. Preconcentration of Proteins on Microfluidic Devices Using Porous Silica Membranes. *Anal. Chem.* **2005**, *77*, 57–63.
4. Song, S.; Singh, A. K.; Kirby, B. J. Electrophoretic Concentration of Proteins at Laser-Patterned Nanoporous Membranes in Microchips. *Anal. Chem.* **2004**, *76*, 4589–4592.
5. Wang, Y.-C.; Han, J. Pre-Binding Dynamic Range and Sensitivity Enhancement for Immuno-Sensors Using Nanofluidic Preconcentrator. *Lab Chip* **2008**, *8*, 392–394.
6. Meagher, R. J.; Hatch, A. V.; Renzi, R. F.; Singh, A. K. An Integrated Microfluidic Platform for Sensitive and Rapid Detection of Biological Toxins. *Lab Chip* **2008**, *8*, 2046–2053.
7. Lee, J. H.; Cosgrove, B. D.; Lauffenburger, D. A.; Han, J. Microfluidic Concentration-Enhanced Cellular Kinase Activity Assay. *J. Am. Chem. Soc.* **2009**, *131*, 10340–10341.
8. Kim, S. J.; Song, Y. A.; Han, J. Nanofluidic Concentration Devices for Biomolecules Utilizing Ion Concentration Polarization: Theory, Fabrication, and Applications. *Chem. Soc. Rev.* **2010**, *39*, 912–922.
9. Zhou, K.; Perry, J. M.; Jacobson, S. C. Transport and Sensing in Nanofluidic Devices. *Annu. Rev. Anal. Chem.* **2011**, *4*, 321–341.
10. Kim, S. J.; Wang, Y.-C.; Lee, J. H.; Jang, H.; Han, J. Concentration Polarization and Nonlinear Electrokinetic Flow near a Nanofluidic Channel. *Phys. Rev. Lett.* **2007**, *99*, 044501.
11. Das, S.; Dubsky, P.; van den Berg, A.; Eijkel, J. C. T. Concentration Polarization in Translocation of DNA through Nanopores and Nanochannels. *Phys. Rev. Lett.* **2012**, *108*, 138101.
12. Zangle, T. A.; Mani, A.; Santiago, J. G. Theory and Experiments of Concentration Polarization and Ion Focusing at Microchannel and Nanochannel Interfaces. *Chem. Soc. Rev.* **2010**, *39*, 1014–1035.
13. Dutzler, R.; Campbell, E. B.; Cadene, M.; Chait, B. T.; MacKinnon, R. X-Ray Structure of a Clc Chloride Channel at 3.0 A Reveals the Molecular Basis of Anion Selectivity. *Nature* **2002**, *415*, 287–294.
14. Owsianik, G.; Talavera, K.; Voets, T.; Nilius, B. Permeation and Selectivity of TRP Channels. *Annu. Rev. Physiol.* **2006**, *68*, 685–717.
15. Venkatachalam, K.; Montell, C. TRP Channels. *Annu. Rev. Biochem.* **2007**, *76*, 387–417.
16. Dunlop, J.; Bowlby, M.; Peri, R.; Vasilyev, D.; Arias, R. High-Throughput Electrophysiology: An Emerging Paradigm for Ion-Channel Screening and Physiology. *Nat. Rev. Drug Discovery* **2008**, *7*, 358–368.
17. Porter, M. C. Concentration Polarization with Membrane Ultrafiltration. *Prod. R&D* **1972**, *11*, 234–248.
18. Song, L.; Elimelech, M. Theory of Concentration Polarization in Crossflow Filtration. *J. Chem. Soc., Faraday Trans.* **1995**, *91*, 3389–3398.
19. Hlushkou, D.; Dhopeshwarkar, R.; Crooks, R. M.; Tallarek, U. The Influence of Membrane Ion-Permselectivity on Electrokinetic Concentration Enrichment in Membrane-Based Preconcentration Units. *Lab Chip* **2008**, *8*, 1153–1162.
20. Pu, Q. S.; Yun, J. S.; Temkin, H.; Liu, S. R. Ion-Enrichment and Ion-Depletion Effect of Nanochannel Structures. *Nano Lett.* **2004**, *4*, 1099–1103.
21. Nguyen, Q. H.; Ali, M.; Bayer, V.; Neumann, R.; Ensinger, W. Charge-Selective Transport of Organic and Protein Analytes through Synthetic Nanochannels. *Nanotechnology* **2010**, *21*, 365701.
22. Yu, Q.; Silber-Li, Z. Measurements of the Ion-Depletion Zone Evolution in a Micro/Nano-Channel. *Microfluid. Nanofluid.* **2011**, *11*, 623–631.
23. Höltzel, A.; Tallarek, U. Ionic Conductance of Nanopores in Microscale Analysis Systems: Where Microfluidics Meets Nanofluidics. *J. Sep. Sci.* **2007**, *30*, 1398–1419.
24. Hatch, A. V.; Herr, A. E.; Throckmorton, D. J.; Brennan, J. S.; Singh, A. K. Integrated Preconcentration SDS−PAGE of Proteins in Microchips Using Photopatterned Cross-Linked Polyacrylamide Gels. *Anal. Chem.* **2006**, *78*, 4976–4984.
25. Sommer, G. J.; Mai, J.; Singh, A. K.; Hatch, A. V. Microscale Isoelectric Fractionation Using Photopolymerized Membranes. *Anal. Chem.* **2011**, *83*, 3120–3125.
26. de Lima, S.; Murad, M.; Moyne, C.; Stemmelen, D. A Three-Scale Model for pH-Dependent Steady Flows in 1:1 Clays. *Acta Geotech.* **2008**, *3*, 153–174.
27. Wang, J.; Gonzalez, A. D.; Ugaz, V. M. Tailoring Bulk Transport in Hydrogels through Control of Polydispersity in the Nanoscale Pore Size Distribution. *Adv. Mater.* **2008**, *20*, 4482–4489.
28. Buckler, K. J.; Vaughan-Jones, R. D. Application of a New pH-Sensitive Fluoroprobe (Carboxy-SNARF-1) for Intracellular pH Measurement in Small, Isolated Cells. *Pflugers Arch.* **1990**, *417*, 234–239.

29. Martinez-Zaguilan, R.; Martinez, G. M.; Lattanzio, F.; Gillies, R. J. Simultaneous Measurement of Intracellular pH and Ca^{2+} Using the Fluorescence of SNARF-1 and FURA-2. *Am. J. Physiol.* **1991**, *260*, C297–307.
30. Timperman, A.; Tracht, S. E.; Sweedler, J. V. Dynamic on-Column pH Monitoring in Capillary Electrophoresis: Application to Volume-Limited Outlet Vials. *Anal. Chem.* **1996**, *68*, 2693–2698.
31. Suss, M. E.; Mani, A.; Zangle, T. A.; Santiago, J. G. Electro-osmotic Pump Performance is Affected by Concentration Polarizations of Both Electrodes and Pump. *Sens. Actuators, A* **2011**, *165*, 310–315.
32. Robinson, H. W. The Influence of Neutral Salts on the pH of Phosphate Buffer Mixtures. *J. Biol. Chem.* **1929**, *82*, 775–802.
33. Hecht, A. H.; Sommer, G. J.; Durland, R. H.; Yang, X.; Singh, A. K.; Hatch, A. V. Aptamers as Affinity Reagents in an Integrated Electrophoretic Lab-on-a-Chip Platform. *Anal. Chem.* **2010**, *82*, 8813–8820.
34. Renzi, R. F.; Stamps, J.; Horn, B. A.; Ferko, S.; VanderNoot, V. A.; West, J. A. A.; Crocker, R.; Wiedenman, B.; Yee, D.; Fruetel, J. A. Hand-Held Microanalytical Instrument for Chip-Based Electrophoretic Separations of Proteins. *Anal. Chem.* **2004**, *77*, 435–441.